Editors' Suggestion

Skyrmions in nanorings: A versatile platform for skyrmionics

Dimitris Kechrakos,[1,*] Vito Puliafito,[2] Alejandro Riveros,[3,4] Jiahao Liu,[5,6,7] Wanjun Jiang,[5,6] Mario Carpentieri,[2] Riccardo Tomasello,[2,†] and Giovanni Finocchio[4,‡]

[1] *Physics Laboratory, Department of Education, School of Pedagogical and Technological Education (ASPETE), Athens, Greece*
[2] *Department of Electrical and Information Engineering, Technical University of Bari, Bari, 70125, Italy*
[3] *Escuela de Ingeniería, Universidad Central de Chile, Santiago, 8330601, Chile*
[4] *Department of Mathematical and Computer Sciences, Physical Sciences and Earth Sciences, University of Messina, Messina, I-98166, Italy*
[5] *State Key Laboratory of Low-Dimensional Quantum Physics and Department of Physics, Tsinghua University, Beijing, 100084, China*
[6] *Frontier Science Center for Quantum Information, Tsinghua University, Beijing, 100084, China*
[7] *College of Advanced Interdisciplinary Studies & Hunan Provincial Key Laboratory of Novel Nano-Optoelectronic Information Materials and Devices, National University of Defense Technology, Changsha, Hunan 410073, China*

(Received 21 June 2023; accepted 25 September 2023; published 16 October 2023)

The dynamical properties of skyrmions can be exploited to build devices with new functionalities. Here, we first investigate a skyrmion-based ring-shaped device by means of micromagnetic simulations and Thiele's equation. We subsequently show three application scenarios: (1) a clock with tunable frequency that is biased with an electrical current having a radial spatial distribution, (2) an alternator, where the skyrmion circular motion driven by an engineered anisotropy gradient is converted into an electrical signal, and (3) an energy harvester, where the skyrmion motion driven by a thermal gradient is converted into an electrical signal, thus providing a heat recovery operation. We also show how to precisely tune the frequency and amplitude of the output electrical signals by varying material parameters, geometrical parameters, and number and velocity of skyrmions, and we further prove the correct device functionality under realistic conditions of room temperature and internal material defects. Our results open an alternative route for the realization of energy efficient nanoscale clocks, generators, and energy harvesters.

DOI: 10.1103/PhysRevApplied.20.044039

I. INTRODUCTION

Magnetic skyrmions are fascinating topological textures with a number of intriguing fundamental properties and several potential engineering applications. Skyrmions are characterized by an integer topological index (skyrmion number) $Q = 1/4\pi \int \mathbf{m} \cdot (\partial_x \mathbf{m} \times \partial_y \mathbf{m}) dxdy$ [1,2], which represents the number of times the magnetization vector wraps a surface of the unit sphere. Topologically, skyrmion transformation into a phase with a different Q is forbidden from a mathematical point of view [1,2]. However, physically, such a "topological protection" provides an additional barrier for skyrmion annihilation and/or nucleation [3,4].

In view of skyrmion-based technological applications, two crucial requirements are necessary: electrical control and room-temperature stability of skyrmions. So far, skyrmion manipulation by spin-orbit torque (SOT) is the most frequently studied approach [5–10]. However, promising alternative methods have also been proposed. Some of these are based on gradients of the external magnetic field [11–14], perpendicular anisotropy [15,16], and thermal gradient (skyrmion caloritronics) [17–19]. Room-temperature skyrmionic states have been observed in a wide range of materials, such as B20 compounds [20,21], a ferromagnetic (FM) single layer in contact with a heavy metal (HM) [10,22,23], HM1/FM/HM2 ferromagnetic multilayers [8,9,24–29], ferrimagnets [30,31], synthetic antiferromagnets (SAFs) [32–34], and combinations of these [35–37].

A prime application of skyrmions is the racetrack memory that has stimulated a lot of research efforts [38–40]. In these devices, the digital information can be coded in the presence or absence of a skyrmion or in two different types of skyrmions [35,37,41]. However, skyrmion racetrack memory suffers from a big drawback, intrinsically linked

*dkehrakos@aspete.gr
†riccardo.tomasello@poliba.it
‡gfinocchio@unime.it

 © 2023 American Physical Society

to the topological character of ferromagnetic skyrmions, which is the occurrence of a finite skyrmion Hall angle [9,10,42] that quantifies the undesired drag of skyrmions in a direction that is transverse to the racetrack. Many strategies have been proposed to reduce and ultimately suppress the skyrmion Hall angle, from engineering anisotropy in ferromagnetic tracks [15,43,44] to the use of ferrimagnets [30] and antiferromagnets [45–48], including SAFs [49,50]. Predicted conventional applications also include spin-torque oscillators [51–54], microwave detectors [55], and logic gates [56–58]. Furthermore, skyrmions have been suggested for unconventional applications, such as in a reshuffle device for probabilistic computing [59,60], reservoir computing [61–63], true random number generators [64], Boolean logic computing gates [56,65–67], neuromorphic computing [68,69], artificial spiking neurons [70,71], memristive networks [72–74], and for solving the shortest path problem [75].

A promising geometry for skyrmion-based devices is a nanoring, where skyrmions have been previously studied experimentally with respect to their field gradient–driven motion [12], and theoretically for microwave emissions [76], and controlled nucleation [77]. Here, we expand the potential usage of such structures by designing three applications: (1) a clock with tunable frequency, (2) a skyrmion-alternator, and (3) a skyrmion-based energy harvester. We first demonstrate these functionalities by means of massive micromagnetic simulations and analytical calculations based on Thiele formalism. Subsequently, we propose their potential experimental implementations.

The working principle of the skyrmion clock (device 1) is based on the usage of a nanoring to generate a periodic electrical signal by repeatedly passing skyrmions through a detector region of the nanoring. Skyrmion motion is induced via standard SOT originating from a spin current with a radial distribution. Skyrmion detection can be achieved via either the topological Hall resistivity [27,28,78] or the tunneling magnetoresistance (TMR) [79,80]. These devices allow not only for frequency tunability via the number of skyrmions circulating in the nanoring, but also for precise tunability based on injected current and/or material parameters.

The skyrmion alternator (device 2) is realized with a contactless detection via a Faraday coil. The time variation of the stray field, generated by the periodic passage of the skyrmion under the Faraday coil, generates an electrical ac voltage with an amplitude proportional to the skyrmion velocity. As we demonstrate in the present work, for a set of parameters corresponding to state-of-the-art skyrmionic materials, the generated voltage amplitude can reach values of the order of 1 μV. In such an application, to increase the energy conversion efficiency, we envisage a skyrmion motion driven by an engineered magnetic anisotropy [15,16], which can be considered as an ultralow-power driving mechanism. The skyrmion alternator is an important prediction of our work since it represents the standard approach used in today's technology for the generation of electrical energy, which can be potentially used to drive nano or micro machines.

The skyrmion energy harvester (device 3) is based on the partial conversion of thermal energy due to heat dissipation into electrical energy. We envisage the presence of a heat source, for example, a microprocessor, located at the center of the nanoring. The thermal energy is dissipated towards the outer part of the nanoring thus creating a thermal gradient. The latter can trigger the skyrmion motion that is converted into an output voltage when the skyrmion passes underneath a Faraday coil. Considering also the feature of zero input energy for gradient-driven motion, the suggested skyrmion application represents a very promising path towards the on-chip conversion from skyrmion motion and dissipated heat into electricity. We also prove the stable operation of device 1 under the influence of thermal fluctuations and internal material defects, and the robustness we demonstrate is also valid for the device 2 and 3 schemes.

II. DEVICE AND MODELING

A. Device description

Figure 1(a) shows the proposed device for the skyrmion clock with tunable frequency. It is composed of an FM nanoring on top of an extended HM layer, with two gold contacts (yellow in the figure); one is inside the nanoring and the other surrounds the nanoring. The nanoring has external diameter d_{NR}, track width w, and thickness t_{FM}. Typical material parameters are chosen to stabilize Néel skyrmions [39,81]. The driving force is a nonuniform radial charge current j flowing into the HM that varies along the radial directions as $j_{\mathrm{HM}}(r) = j R_0/r$, where j is the injected current density and R_0 the inner radius of the nanoring. The current density generates an SOT with a counterclockwise circular spin polarization **p** [39]. The skyrmion dynamics are characterized by a circular trajectory [see red curve in Fig. 1(a)] where the radial motion due to the skyrmion Hall angle [42] is almost compensated by the confining potential [39]. For this choice, the current-induced skyrmion Hall effect leads to a weakly inward trajectory of the skyrmions that causes their eventual annihilation at the inner boundary of the nanoring at large currents. The choice of an outward trajectory is less preferable, since the skyrmions would gradually enter regions of the nanoring with lower current density that would halt their motion. The device is equipped with a detector that is based on an magnetic tunnel junction (MTJ) with width $w_d = 60$ nm and a length equal to the width w of the nanoring. Note that the detector can also be implemented with elliptical or circular geometry. The detector width w_d is designed to be larger than the single skyrmion size considered (skyrmion diameter $D_{\mathrm{sk}} \approx 35$–40 nm) to achieve

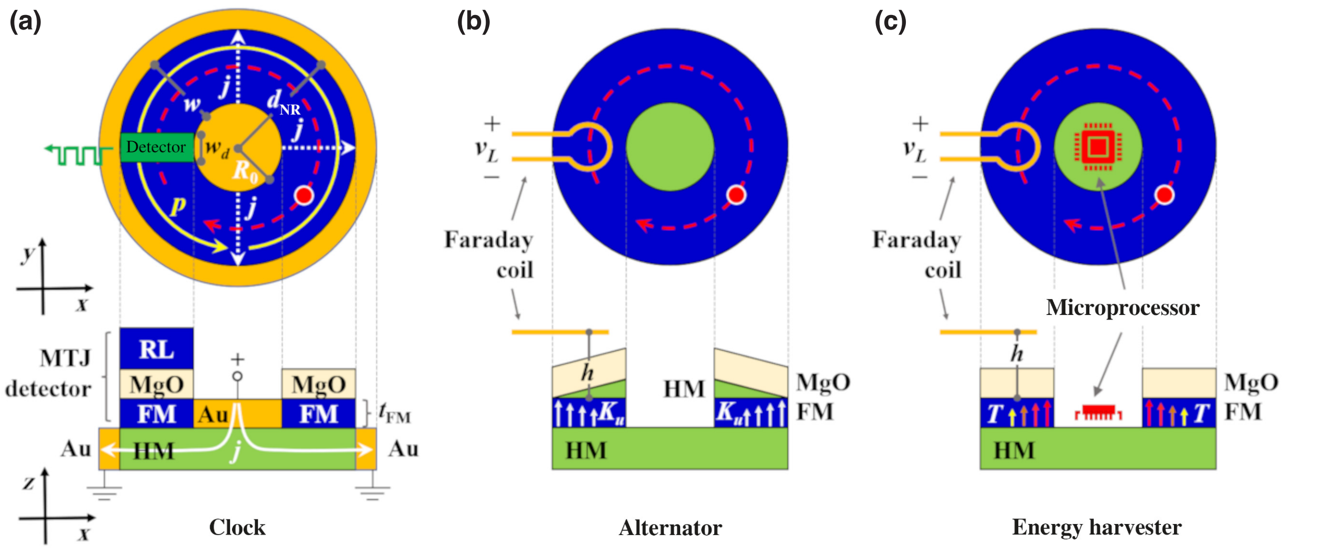

FIG. 1. Schematic representations of the skyrmion in a nanoring for the three applications envisaged in this work. (a) Clock with tunable frequency where the skyrmion circular motion is driven by an electrical current j flowing between the internal and external Au electrodes via the HM (radial distribution of the current, circular distribution of the spin-polarization **p**). The skyrmion is detected via a localized MTJ, which has the FM as its free layer, and converts the variation of the out-of-plane magnetization into an electrical pulse. (b) Alternator where the skyrmion circular motion is driven by a perpendicular anisotropy gradient due to insertion of the HM wedged layer, as in Ref. [15]. The free-energy-driven motion of the skyrmion is converted into an electrical pulse v_L by the Faraday coil located at a distance h from the FM surface. The bottom HM is necessary only to reach a finite IDMI value. (c) Energy harvester where the skyrmion circular motion is promoted by a thermal gradient generated by a thermal source, e.g., a microprocessor, located in the middle of the nanoring. As in (b), the skyrmion motion is converted into an electrical pulse v_L by the Faraday coil, and the bottom HM is necessary only to reach a finite IDMI value. RL, reference layer.

an efficient detection. The presence of a skyrmion in the detector region leads to variation of the magnetoresistive signal of the MTJ [79,80,82]. Moreover, this scheme allows for generating a clock signal in different positions of the nanotrack thanks to additional MTJ detectors and because the skyrmion is moving at the same velocity along the nanoring. In other words, we can achieve an intrinsic spatial synchronization of the clock frequency.

Figures 1(b) and 1(c) show the proposed devices for the skyrmion alternator and energy harvester, respectively. Geometrically, these are similar to the previous device, but here the extended HM is necessary only to provide a sufficiently large interfacial Dzyaloshinskii-Moriya interaction (IDMI). The skyrmion motion is promoted by an engineered perpendicular anisotropy radial gradient (device 2) and a thermal radial gradient (device 3). The skyrmion motion in converted into an output electrical voltage v_L when skyrmions pass below a Faraday coil [yellow circle in Figs. 1(b) and 1(c)] located at height h from the nanoring surface due to the well-known Faraday-Neumann-Lenz effect $v_L = -d\Phi/dt$, where $d\Phi$ represents the flux variation generated by the skyrmion movement below the coil. Table I summarizes the three proposed applications.

B. Micromagnetic model

The device design is based on massive micromagnetic simulations performed by means of the state-of-the-art micromagnetic solver PETASPIN, which numerically integrates the Landau-Lifshitz-Gilbert equation, augmented by the Slonczewski SOT term [83,84],

$$\frac{d\mathbf{m}}{d\tau} = \mathbf{m} \times \mathbf{h}_{\text{eff}} + \alpha_G \left(\mathbf{m} \times \frac{d\mathbf{m}}{d\tau}\right) - \frac{g\mu_B\theta_{\text{SH}}}{2\gamma_0 e M_s^2 t_{\text{FM}}}[\mathbf{m} \times (\mathbf{m} \times (\hat{\mathbf{z}} \times \mathbf{j}_{\text{HM}}))], \quad (1)$$

TABLE I. Summary of the versatile applications for skyrmions in nanoring.

Application	Source of skyrmion motion	Detection or conversion
Skyrmion clock (device 1)	SOT with a tangential spin-polarization (**p**)	Magnetoresistive effect in MTJ
Skyrmion alternator (device 2)	Linear gradient of the perpendicular anisotropy	Faraday coil
Energy harvester (device 3)	Linear thermal gradient	Faraday coil

where $\mathbf{m} = \mathbf{M}/M_s$ is the normalized magnetization, $\tau = \gamma_0 M_s t$ is the dimensionless time, with γ_0 being the gyromagnetic ratio and M_s the saturation magnetization. $\mathbf{h}_{\text{eff}}$ is the dimensionless effective field that includes the external, exchange, IDMI, magnetostatic, and perpendicular anisotropy fields. α_G is the Gilbert damping, g is the Landé factor, μ_B is the Bohr magneton, θ_{SH} is the spin Hall angle, e is the electron charge, t_{FM} is the thickness of the ferromagnetic layer, $\hat{\mathbf{z}}$ is the unit vector along the out-of-plane direction, and $\mathbf{j}_{\text{HM}}$ is the electrical current density flowing through the HM layer and giving rise to the SOT. The results presented here are for skyrmions in a nanoring with external diameter $d_{\text{NR}} = 460$ nm, width $w = 150$ nm, and thickness $t_{\text{FM}} = 1$ nm. Similar qualitative results are also observed for different nanoring sizes. We discretize the ring with cell dimensions $2 \times 2 \times 1$ nm^3. We use the following parameters, unless indicated otherwise [39]: $M_s = 600$ kA/m, exchange constant $A = 10$ pJ/m, IDMI parameter $D_m = 1.8$ mJ/m^2, perpendicular anisotropy constant $K_u = 0.80$ MJ/m^3, spin Hall angle $\theta_{\text{SH}} = 0.33$, and $\alpha_G = 0.01$.

C. Thiele's equation

The analytical description of the skyrmion dynamics in the nanoring for the three device mechanisms can be achieved by the Thiele equation [39,85],

$$\mathbf{G} \times \mathbf{v} - \alpha_G D \cdot \mathbf{v} + \mathbf{F}_{\text{SOT}} + \mathbf{F}_K + \mathbf{F}_T = 0, \quad (2)$$

where $\mathbf{G} = G\hat{\mathbf{z}}$ is the gyrovector, $\mathbf{v}$ the skyrmion (core) velocity, and D the dissipative tensor matrix, respectively, while $\mathbf{F}_{\text{SOT}}$ is the force due to the SOT with tangential spin polarization (device 1), $\mathbf{F}_K$ the force due to the radial gradient of perpendicular anisotropy (device 2), and $\mathbf{F}_T$ the force due to the radial temperature gradient (device 3).

In particular, $\mathbf{F}_{\text{SOT}} = 4\pi B\, \mathbf{j}_{\text{HM}}$, where $\mathbf{j}_{\text{HM}}(r) = (j R_0/r)\hat{\mathbf{r}}$ is the radially symmetric charge current density, $B = g\mu_B \theta_{\text{SH}}/2\gamma_0 e {M_s}^2 t_{\text{FM}}$ multiplied by a scaling factor to allow for racetrack shape effects [39], and R_0 the internal radius of the nanoring. On the other hand, the forces due to anisotropy and thermal gradient for devices 2 and 3 can be calculated through derivatives of the effective potential V_{eff} associated with the effective field $\mathbf{h}_{\text{eff}}$ as obtained from the effective field theory [19],

$$V_{\text{eff}} = 2\pi \left(4A \left(\frac{\Delta}{R_{sk}} + \frac{R_{sk}}{\Delta} \right) + 4K\,\Delta - 2\pi\, D_m R_{sk} \right), \quad (3)$$

where $\Delta = \sqrt{A/K}$ is the domain wall width, $R_{\text{sk}} = \Delta/\sqrt{2\left(1 - \left(\pi D_m/4\sqrt{AK}\right)\right)}$ the equilibrium skyrmion radius, $K = K_u - \mu_0 M_s^2/2$ the effective magnetic anisotropy strength within the thin-film approximation, and D_m and K_u are the IDMI parameter and perpendicular anisotropy strength. Note that V_{eff} is spatially uniform for device 1. Nevertheless, for device 2 it varies as $K_u = a_K\, r + b_K$ leading to a radially dependent potential $V_{\text{eff}} = V_{\text{eff}}(r)$, which induces the force due to anisotropy gradient as

$$\mathbf{F}_K = -\frac{\hat{\mathbf{r}}}{\mu_0 M_s^2} a_K \frac{\partial V_{\text{eff}}}{\partial K} = \hat{\mathbf{r}} F_K(r), \quad (4)$$

with a_K the anisotropy gradient. Similarly, for device 3 we assume a temperature gradient in the radial direction, $T = a_T\, r + b_T$. We allow for temperature-dependent micromagnetic material parameters through the well-established scaling relations [19,81], $M_s \equiv M_s(T) = M_{s0}(1 - (T/T_{\text{lim}})^{\delta})$, $A \equiv A(T) = A_0\, m(T)^{\alpha}$, $D_m \equiv D_m(T) = D_{m0}\, m(T)^{\beta}$, and $K_u \equiv K_u(T) = K_{u0}\, m(T)^{\gamma}$, where $m(T) = M_s(T)/M_{s0}$ and $M_{s0}, A_0, D_{m0}, K_{u0}$ are the corresponding material parameters at zero temperature. The exponents are given as [19,81] $\alpha = \beta = \delta = 3/2$ and $\gamma = 3$, and $T_{\text{lim}} = 1120$ K is the Curie temperature. Eventually, the temperature gradient leads to a temperature-dependent effective potential $V_{\text{eff}} = V_{\text{eff}}(T)$, with a position-dependent temperature $T = T(r)$, and the resultant force due to the temperature gradient in device 3 is

$$\mathbf{F}_T = -\frac{\hat{\mathbf{r}}}{\mu_0 M_s^2} a_T \frac{\partial V_{\text{eff}}}{\partial T} = \hat{\mathbf{r}} F_T(r). \quad (5)$$

Since the three forces $\mathbf{F}_{\text{SOT}}$, $\mathbf{F}_K$, and $\mathbf{F}_T$ are all in the radial direction it is convenient to express Eq. (2) in polar coordinates (r, ϕ) of the skyrmion-core position, which can then be cast in matrix notation in the polar basis as

$$\begin{pmatrix} -\alpha_G D & -G \\ G & -\alpha_G D \end{pmatrix} \begin{pmatrix} \dot{r} \\ r\dot{\phi} \end{pmatrix} = -F(r) \begin{pmatrix} 1 \\ 0 \end{pmatrix}, \quad (6)$$

where $F(r)$ denotes any of the three types of forces $F_{\text{SOT}}(r)$, $F_K(r)$, $F_T(r)$ acting on the skyrmion. From Eq. (6) we obtain for the radial and angular components of the skyrmion velocity,

$$\dot{r} = \alpha_G D\, F(r)/(G^2 + \alpha_G^2 D^2) \text{and}$$
$$r\dot{\phi} = G F(r)/(G^2 + \alpha_G^2 D^2), \quad (7)$$

with the dot sign indicating a derivative with respect to dimensionless time τ. Elimination of time and integration of Eq. (7) provides the skyrmion core trajectory

$$r(\phi) = r_0 \exp[\alpha_G D(\phi - \phi_0)/G], \quad (8)$$

which is a logarithmic spiral for the skyrmion motion in the three devices, and r_0, ϕ_0 are the initial values ($\tau = 0$). Notice that the shape of the skyrmion trajectory, Eq. (8), is independent of the particular functional form of the radial force $F(r)$. On the other hand, the time evolution of the radial and azimuthal components of the skyrmion trajectory depend explicitly on the functional form of $F(r)$, which can be obtained by integrating Eq. (7). Analytical expressions of $F(r)$ are obtained from Eqs. (4) and (5) using a symbolic algebra software.

III. NUMERICAL RESULTS: SKYRMION CLOCK (DEVICE 1)

We discuss first our proposal for a skyrmion clock, where the motion is driven by the SOT from the electrical current and the skyrmion detection is performed via an MTJ detector with perpendicular pinned layer in order to sense, through a change of its resistance, the variation of the out-of-plane spatially averaged magnetization component $\langle m_z \rangle$. In the case of a single skyrmion circulating in the nanoring, the micromagnetic results are summarized in Fig. 2. Clearly, the time evolution of $\langle m_z \rangle$ under the MTJ is characterized by a series of periodic dips ["comb" structure, Figs. 2(a)–2(d)], which occur when the skyrmion passes underneath the detector. Simultaneous with the drop in magnetization, we show that the topological charge in the detector region reaches the value $Q = -1$, signifying the presence of a skyrmion under the MTJ.

The most important feature here is an evident periodicity of the skyrmion signal for up to four to five laps around the nanoring in a time interval up to approximately 200 ns that points to efficient pulse generation with constant frequency. However, we observe two features linked to the interaction of the skyrmion with the internal boundary of the nanoring as it completes more laps: (i) a delay in the last peak of the $\langle m_z \rangle$ signal indicating the slowdown of the skyrmion, and (ii) smaller $\langle m_z \rangle$ variations below the MTJ indicating a skyrmion size reduction, while Q remains the same.

From recording the time instants corresponding to the dips of the $\langle m_z \rangle$ signal, we show that successive skyrmion laps by the detector vary linearly with time in Fig. 2(e). To support the results from micromagnetic simulations, we compare also with the analytical computations with the Thiele's equation described in previous section. For the clock device, $F(r) = F_{\mathrm{SOT}}(r) = 4\pi B j R_0 / r$ and Eq. (7) can be written as

$$\dot{r} = u\,\alpha_G D / G r \text{ and } r\dot{\phi} = u/r, \tag{9}$$

with $u = [4\pi B G/(G^2 + \alpha_G^2 D^2)] R_0 j$. Then the time evolution of the radial and azimuthal components are

$$r(\tau) = \sqrt{r_0^2 + 2u\alpha_G D\tau/G} \text{ and}$$
$$\phi(\tau) = \phi_0 + \frac{G}{2\alpha_G D}\ln\left(1 + \frac{2u\alpha_G D}{G r_0^2}\tau\right). \tag{10}$$

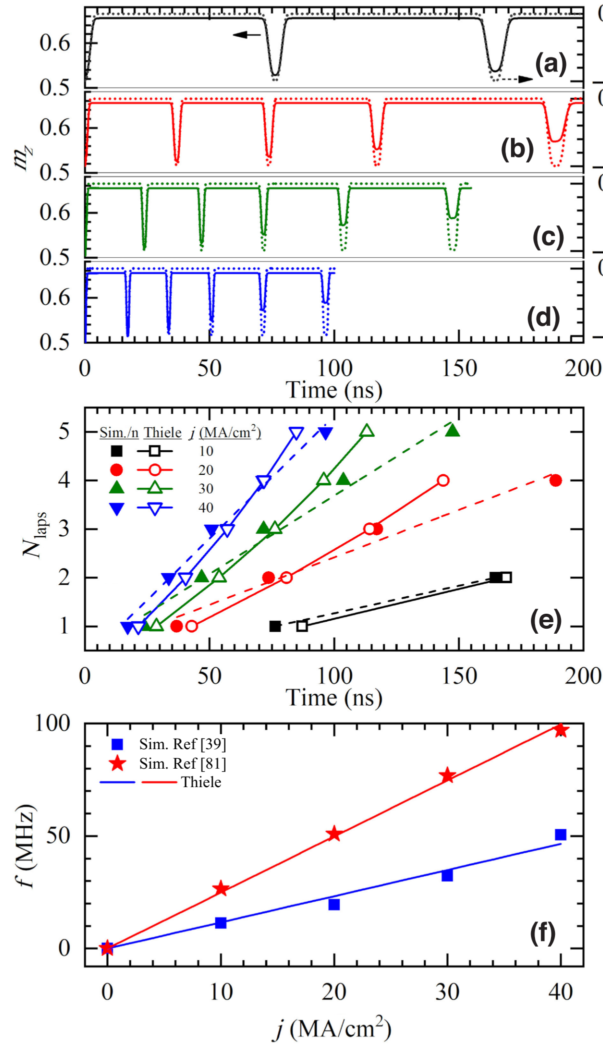

FIG. 2. Single skyrmion in a nanoring driven by an electrical current. (a)–(d) Time evolution of the spatially averaged out-of-plane component of the magnetization (solid lines) and the topological charge (dashed lines) in the detector region for different current densities $j = 10$ (black), 20 (red), 30 (green), and 40 (blue) MA/cm^2, respectively. (e) Number of skyrmion laps in the detector region as a function of the elapsed time for various current densities, as indicated in the legend. A comparison of the analytical model predictions from Eq. (12) for $N_{\mathrm{sk}} = 1$ (open markers) with micromagnetic simulation results (closed markers) is shown. Dashed lines are linear fits of the micromagnetic simulation data for extracting the frequency of the skyrmion motion reported in (f). (f) Dependence of the output signal frequency on the electrical current density. Solid lines are the predictions of the analytical model, Eq. (12), while symbols refer to the micromagnetic simulation results with the parameters provided in Refs. [39,81].

The elapsed time τ_n for a skyrmion to perform n laps through the detector is obtained from Eq. (10) by setting $\phi(\tau_n) = \phi_0 \pm 2\pi n$,

$$\tau_n = \frac{G\,r_0^2}{2\alpha_G D u}\left(e^{\pm 4\pi n \alpha_G D/G} - 1\right), \tag{11}$$

with the upper (lower) sign in the exponential term corresponding to counterclockwise (clockwise) motion of the skyrmion along the spiral trajectory. The frequency (in hertz) of the nth full circle along the spiral is defined as $f_n = (\tau_n - \tau_{n-1})^{-1}$ and becomes

$$f_n = \gamma_0 M_s \frac{2\alpha_G D u}{G r_0^2} e^{\mp 4\pi n \alpha_G D/G}(1 - e^{\mp 4\pi \alpha_G D/G})^{-1}. \quad (12)$$

Note that the ratio of frequencies for successive laps is given by

$$\frac{f_{n+1}}{f_n} = e^{\mp 4\pi \alpha_G D/G}, \quad (13)$$

which implies that the frequency of the generated electrical pulses due to sequential passages of the skyrmion through the detector region is not constant. However, for most FM materials of interest $\alpha_G D/G \ll 1$ and thus, a near constant frequency can be achieved as indicated by Eq. (13). As shown in Figs. 2(e) and 2(f), the analytical and numerical outcomes are in a good agreement for both the skyrmion frequency and its number of laps in the detector region for different current densities and magnetic parameters, where the number of skyrmion laps and frequency predicted by the Thiele formalism are obtained by Eqs. (11) and (12), respectively. A time delay of the laps relative to the predictions of the analytical model is attributed to the skyrmion-boundary interaction that hinders the skyrmion motion. Interestingly, the boundary-free motion under a radial current density predicts a weakly accelerated skyrmion motion (see Sec. III B), but the skyrmion-boundary interaction competes with this effect, eventually restoring a constant velocity [see Fig. 2(e)].

An advantage of this device is its frequency tunability, which can be achieved by changing the driving current density, as indicated by the linear scaling of the frequency with current density in Fig. 2(e), and the number of skyrmions, as discussed in the following paragraph. In addition, the material parameters can be used to set the desired frequency region [39,81] [Fig. 2(f)]. We also wish to highlight that the skyrmion configuration has an intrinsic reset mechanism owing to the magnetostatic interactions that realign the skyrmion position to the center of the nanoring in the absence of an applied current.

The thickness of the ferromagnet can influence different parameters. The most sensitive are the interfacial perpendicular anisotropy, the IDMI, and the amplitude of the SOT. All three contributions scale linearly as a function of the thickness [86,87]. The first two parameters affect the skyrmion stability and, above a certain critical thickness, the skyrmion is no longer stable. In addition, the reduction of the SOT with thickness, for a fixed set of parameters, gives rise to a reduction of the slope of the velocity-current curve. We perform simulations with different values of the ferromagnetic film thickness (from 1.0 to 2.0 nm) keeping a fixed set of parameters (see Sec. III B) and constant current density. Our simulations indicate a drop of frequency of up to 50% when the layer thickness increases from 1.0 to 2.0 nm (not shown here).

A. Clock with multiple skyrmions in the nanoring

Higher pulse frequencies can be achieved when an N-skyrmion ($N_{\rm sk}$) chain is stabilized in the nanoring. In simulations, we place multiple skyrmions in the nanoring and relax the system prior to applying the electrical current. The skyrmions are located at symmetrical points in the device. In particular, for the case of $N_{\rm sk} = 2$, we create the skyrmions on a circle in the half-width of the nanoring at angular positions of 0° and 180° with respect to the detector region and, for the case of $N_{\rm sk} = 4$, we place skyrmions at angular positions of 0°, 90°, 180°, and 270°. Figures 3(a) and 3(b) show the TMR signal due to the passage of multiple skyrmions for a fixed $j = 20$ MA/cm^2 for $N_{\rm sk} = 2$ and $N_{\rm sk} = 4$, respectively, where the decrease of the $\langle m_z \rangle$ period with the number of skyrmions is evident. To support this finding, we depict in Fig. 3(c) the number of laps versus time for different current densities, where the curve slopes for $N_{\rm sk} = 4$ is always larger than the $N_{\rm sk} = 2$ case. Eventually, the previous results are confirmed in Fig. 3(d), where the frequency as a function of the current density for different $N_{\rm sk}$ is shown, thus underlining the role of the number of skyrmions in tuning the working frequency of the device.

The Thiele's equation can be extended to account for $N_{\rm sk}$ skyrmions. In particular, Eq. (12) is also valid in the case of a skyrmion chain composed of $N_{\rm sk}$ equidistant and noninteracting skyrmions circulating on the nanoring. In this case, the detected frequency corresponds to the frequency of a single skyrmion scaled by the number of skyrmions in the chain,

$$f_n(N_{\rm sk}) = N_{\rm sk} f_n(1). \quad (14)$$

However, for a dense skyrmion chain, namely when the core-to-core distance approaches the skyrmion diameter, the detected frequency is anticipated to deviate slightly from the predictions of Eq. (14). The underlying physical mechanism causing these deviations is due to the skyrmion-skyrmion repulsive forces that alter the skyrmion shape and hence the dynamics of the interacting skyrmion chain. Nonetheless, for our study, the analytical predictions are in line with the micromagnetic simulation results. Weak deviations from the constant pulse frequency can be observed for high current density and long times [Fig. 3(c)] due to the interaction of the skyrmion with the inner boundary of the nanoring; however, due to the increased number of skyrmions in the device, a larger number of pulses is generated relative to the single skyrmion case before the linearity is perturbed.

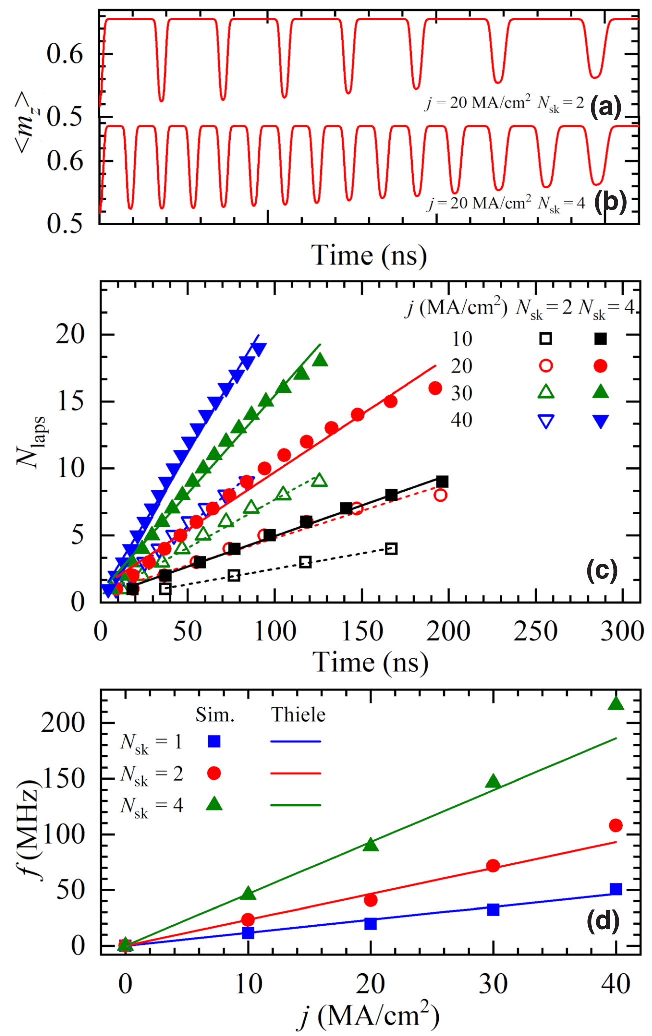

FIG. 3. Time evolution of the spatially averaged out-of-plane component of the magnetization $\langle m_z \rangle$ for (a) two and (b) four skyrmions in the nanoring driven by current density $j = 20$ MA/cm^2. (c) Number of laps in the MTJ detector as a function of the elapsed time for two-skyrmion (open symbols) and four-skyrmion (closed symbols) chains and various driving current densities. Straight lines (dashed for $N_{sk} = 2$, solid for $N_{sk} = 4$) are linear fits to the data used to extract the corresponding frequency values, which are shown as markers in (d). (d) Dependence of the output signal frequency on the electrical current density. Solid lines are the predictions of the analytical model, Eq. (14), while symbols refer to the micromagnetic simulation results.

Noticeably, the overlap of different datasets in Fig. 3(c), as for example the case of two skyrmions under $j = 20$ MA/cm^2 and the case of four skyrmions under $j = 10$ MA/cm^2, demonstrates the equivalence of the two controlling parameters of the pulse frequency, namely the driving current density j and the number of injected skyrmions N_{sk}. We wish to stress again that an important requirement for achieving linear scale-up of the signal frequency is to have the skyrmions equidistant in the device, as nonequidistant skyrmions would generate an electrical pulse with two or more constituent frequencies; for initial states where the skyrmions are not equidistant we observe their rearrangement to the equidistant configuration thanks to the magnetostatic field (not shown) [12].

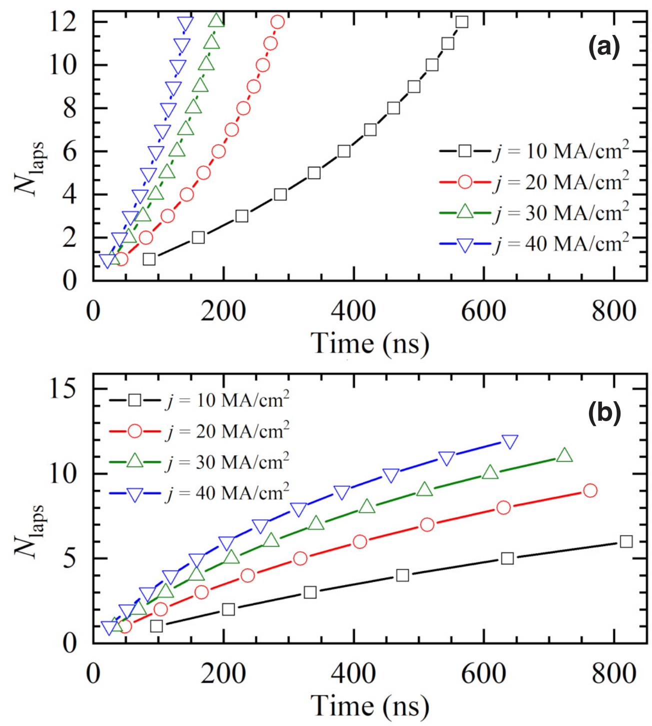

FIG. 4. Number of skyrmion laps in the MTJ detector region as a function of the elapsed time (t_n) given by Eq. (11) for a skyrmion circulating (a) inwards and (b) outwards. At $t = 0$ s, the skyrmion is located at the detector position in the middle of the ring width, that is $r_0 = R_0 + w/2$ and $\phi_0 = \pi$.

B. Extended results of the Thiele's equation

Figure 4 shows the results predicted from the solution of Thiele's equation, Eq. (11), for a larger time interval and the material parameters mentioned earlier [39]. Interestingly, the time evolution of the lap number follows a weak logarithmic dependence, which suggests that, intrinsically, the frequency generated by the skyrmion rotation cannot be constant unless a damping parameter close to zero is considered. However, for an initial time interval (about 200 ns), the relation between the number of laps and time can be quite accurately approximated by a linear dependence that, in turn, implies a constant frequency of motion which is a prerequisite for clock functionality.

C. Effect of sample disorder

Typical FM/HM samples are polycrystalline and include internal defects, which are usually responsible for skyrmion pinning [8,88]. To study the effects of sample defects on the skyrmion circular motion, we divide the

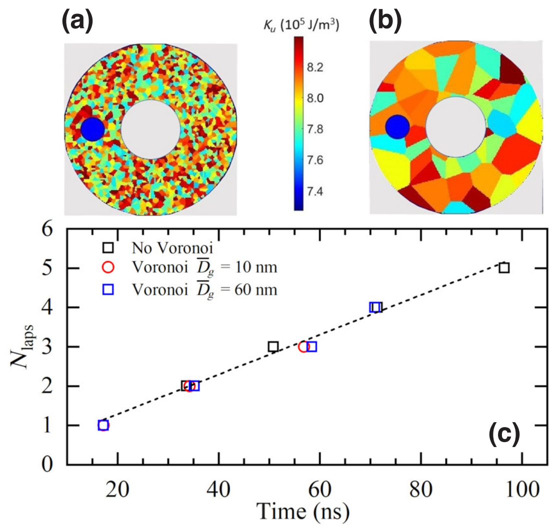

FIG. 5. Examples of Voronoi tessellation for (a) small grains with average size $\bar{D}_g = 10$ nm and (b) large grains with average size $\bar{D}_g = 60$ nm. The blue disk on each nanoring is a sketch of a skyrmion with diameter $D_{\rm sk} \approx 30$ nm. The color-scale bar indicates the values of the perpendicular anisotropy constant. It is characterized by 5% dispersion around the mean value $\bar{K}_u = 0.8$ MJ/m^3. (c) Mean number of skyrmion laps as a function of time for a single skyrmion circulating in an ideal nanoring (black squares) and disordered nanorings (red circles, blue squares). The applied current density is $j = 40$ MA/cm^2 and the average grain size is $\bar{D}_g = 10$ nm (red circles) and $\bar{D}_g = 60$ nm (blue squares). Error bars due to disorder are of the size of the marks. The straight dashed line is a linear fit to all data and serves as a guide to the eye.

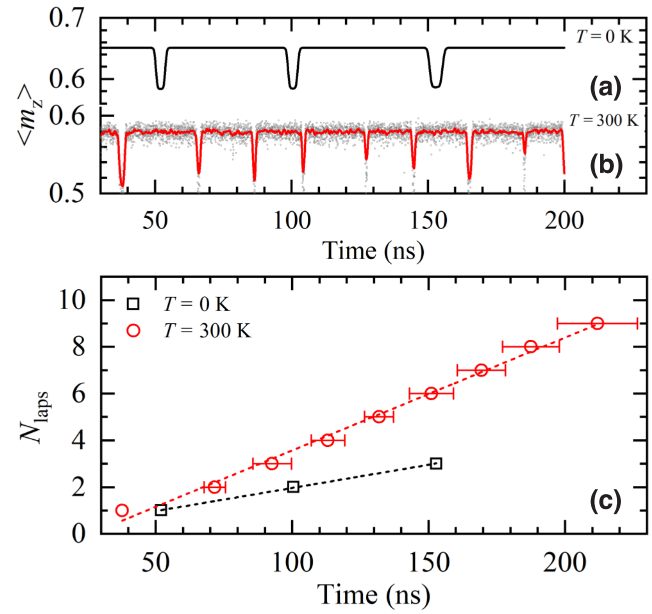

FIG. 6. (a),(b) Time evolution of the out-of-plane component of the magnetization $\langle m_z \rangle$ below the MTJ at $T = 0$ K and $T = 300$ K for a single skyrmion in the nanoring under a driving current density $j = 20$ MA/cm^2. An out-of-plane field ($H_z = 300$ mT) and a slightly stronger IDMI value ($D_m = 4$ mJ/m^2) is used in order to stabilize the skyrmion at the elevated temperature ($T = 300$ K). Gray markers in (b) indicate the raw noisy signal while the solid red line refers to the smooth signal, as obtained by a running-average method with a time window of 1 ns. (c) Number of skyrmion laps in the detector region as a function of time at $T = 0$ K (squares) and $T = 300$ K (open red circles with corresponding error bars). Straight dashed lines are linear fits to data.

nanoring in regions of random shape and size (grains) implementing the Voronoi tessellation algorithm [88]. We attribute a random value to the perpendicular anisotropy K_u of each grain with a dispersion of 5% around the mean value. In addition to the dispersion in anisotropy values, another important parameter in polycrystalline samples is the ratio of the mean grain size $\bar{D}_g$ to the skyrmion diameter $D_{\rm sk}$ [50], which in our simulations is set to $D_{\rm sk} = 30$nm. Figure 5 shows the results for the mean value of the number of skyrmion laps as a function of time. The average is extracted with five different Voronoi maps with $\bar{D}_g$ equal to 10 and 60 nm. We fix $j = 40$ MA/cm^2, which gives the largest frequency of the output signal in the ideal sample [Fig. 2(f)]. Our results demonstrate that for both small and large grain size the effect of the internal defects is negligible, thus proving the robustness of this application to structural disorder.

D. Effect of thermal fluctuations

Temperature effects are important factors introducing randomness in the dynamics of skyrmion motion [60,82,89]. The thermal effects are accounted for in Eq. (1) via a stochastic field $\mathbf{h}_{\rm th}$, that is applied at each computational cell and reads $\mathbf{h}_{\rm th} = (\boldsymbol{\chi}/M_s)\sqrt{2\alpha_G k_B T/\mu_0\gamma_0\Delta V M_s \Delta t}$, with k_B being the Boltzmann constant, ΔV the volume of the computational cubic cell, Δt the simulation time step, T temperature of the sample, and $\boldsymbol{\chi}$ a three-dimensional white Gaussian noise with zero mean and unit variance [90,91]. Values of stochastic field in different cells are uncorrelated. Figure 6 compares the $\langle m_z \rangle$ for a single skyrmion in the nanoring at $T = 0$ K with a typical signal at $T = 300$ K. The latter is noisy due to random thermal fluctuations and a running-average method with a time window of 1 ns is used to extract the smooth signal.

Figure 6(c) shows the number of skyrmion laps as a function of time. The frequency $\bar{f}$ at $T = 300$ K is averaged over ten repetitions over the thermal disorder and the corresponding dispersion is illustrated by the horizontal error bars. The micromagnetic results predict an average frequency $\bar{f} = 49$ MHz at $T = 300$ K, which is more than twice the frequency $f = 20$ MHz at $T = 0$ K. Examination of the magnetization snapshots show that, in the early stage of the motion (up to around 20 ns), the skyrmion develops an outward radial velocity that drives it to the outer boundary, where it continues the circular motion with a higher velocity. We attribute this higher velocity to the synergy between the current-driven motion and the temperature-driven gyrotropic motion of the skyrmions that has been previously studied in nanodots [81]. We also check that the width of the nanoring does not modify this behavior by performing simulations in wider nanorings ($d_{\mathrm{NR}} = 460$ nm, $w_d = 190$ nm), which produce similar frequency enhancement results. Therefore, not only can our proposed application work at room temperature, but the performance in terms of achievable frequency is also better.

IV. NUMERICAL RESULTS: SKYRMION ALTERNATOR AND SKYRMION ENERGY HARVESTER

The second part of the work is dedicated to the design of a skyrmion alternator and a skyrmion energy harvester. Both applications share the same geometry [Figs. 1(b) and 1(c)] and working principle for reading the signal, but have different driving mechanisms for the skyrmion circulating motion. In particular, here it is driven by gradients in the parameters (anisotropy, temperature), and not by an electrical current.

A. Skyrmion alternator

For the skyrmion alternator, we consider a free-energy input source related to the presence of an engineered linear perpendicular anisotropy gradient. Its effect in extended FMs has already been analyzed experimentally and theoretically [15,16], thus making it a viable alternative to the electrical current. In particular, the nanoring-shaped FM can be designed to have a radial gradient of the K_u [see Fig. 1(b) for more details]. Based on our previous results [16], where skyrmions move mainly perpendicularly to the K_u gradient direction, we expect the skyrmion to circulate in the nanoring, and, every time it passes underneath a Faraday coil, the time variation of the stray field flux Φ is converted into a voltage pulse at the terminal of the coil due to the well-known Faraday-Neumann-Lenz effect $v_L = -d\Phi/dt$. In other words, the skyrmion rotation gives rise to an ac voltage, similar to what occurs in the majority of today's electrical generators, where the mechanical rotation of a rotor generates an ac voltage.

B. Skyrmion energy harvester

The skyrmion motion in the energy harvester is instead promoted by a linear temperature gradient [Fig. 1(c)]. Thermal gradients have already been proved to be a reliable motion source for skyrmions [17,19]. In particular, previous theoretical results pointed out that thermal gradients can be taken into account via linear gradients of the magnetic parameters (A, D_m, K_u, M_s) computed with proper scaling relations with temperature [19] [see Sec. II C before Eq. (5)]. The combinations of all the parameters' gradients give rise to a skyrmion motion mostly perpendicular to the gradient direction. With this in mind, our idea is to build the skyrmion-based nanoring around a thermal source, such as a microprocessor [Fig. 1(c)]. Then, the dissipated thermal energy propagates radially towards the outer boundary of the nanoring, and we assume that the heat propagation induces a linear temperature gradient (hotter on the inside and colder on the outside), which is expected to drive the circular motion of the skyrmions. Similar to the case of the skyrmion alternator, this motion can be converted into an ac voltage. In other words, the proposed skyrmion energy harvester can partially recover dissipated heat in the form of electrical energy. Here, we are considering a point source for the thermal gradient in order to have a radial distribution; however, the concept is also applicable for the arbitrary spatial distribution of thermal sources, which would generate, however, nonperiodic output signals across the coil.

C. Conversion of the skyrmion motion into an electrical signal

For both cases of the skyrmion alternator and the skyrmion harvester, we are only interested in the maximum skyrmion velocity for given material parameters, since that determines the value of the generated voltage pulse. Therefore, we do not consider the effect of thermal fluctuations or internal material defects, which we expect to modify our results quantitatively (see Secs. III C and III D), e.g., a smaller skyrmion velocity, but not qualitatively.

To this aim, we develop a postprocessing tool for the calculation of the voltage pulse $v_L = -d\Phi/dt$ generated by the skyrmion motion. As a first step, we perform micromagnetic simulations with the parameters as in Ref. [81]. For the K_u gradient, we consider a minimum (maximum) value at the inner (outer) edge of the nanoring equal to 0.6 MJ/m^3 (0.8 MJ/m^3). For the thermal gradient, we consider a minimum (maximum) value at the outer (inner) edge of the nanoring equal to 100 K (300 K). In both cases, the skyrmion rotates in the nanoring with a velocity $v_{\mathrm{sk}} \approx 20$ m/s. These simulations are needed to: (i) confirm a steady-state size of the skyrmion while moving, and (ii) use that value of the skyrmion velocity as a reference for the postprocessing tool in order to predict how the generated voltage changes with the velocity around that value (see Fig. 7). We compute the spatial distribution of the stray field due to the skyrmion up to 50 nm away from the nanoring surface, and consider a Faraday coil with a diameter similar to the skyrmion one.

Figure 7(a) shows the change of the stray field flux through the Faraday coil located at height $h = 20$ nm from the surface of the nanoring due to the passage of a skyrmion below it. The flux Φ becomes negative as the

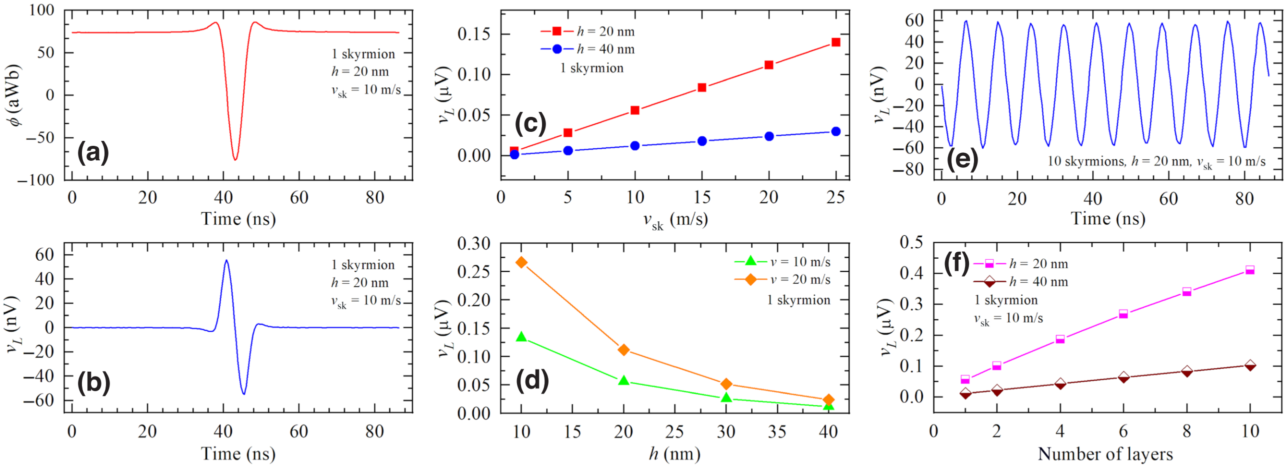

FIG. 7. The ac voltage generated at the terminals of a Faraday coil due to skyrmion circulating motion. (a) Magnetostatic flux time variation corresponding to a passage of one skyrmion underneath the coil for a skyrmion velocity $v_{\mathrm{sk}} = 10$ m/s and a coil height $h = 20$ nm. (b) Generated voltage pulse due to the flux variation in (a). (c) Amplitude of the voltage pulse as a function of the skyrmion velocity for two heights of the coil. (d) Amplitude of the voltage pulse as a function of the coil height for two skyrmion velocities. (e) Steady-state ac voltage output due to the consecutive passage of ten skyrmions below the coil. (f) Amplitude of the voltage pulse as a function of the number of layers of the nanoring FM for two coil heights when $v_{\mathrm{sk}} = 10$ m/s.

skyrmion enters the region below the coil, and symmetrically goes back to a positive value as the skyrmion exits the coil region. The negative flux value is due to the skyrmion polarity, which is negative in this study ($-z$ direction). The corresponding nanovolt voltage pulse is illustrated in Fig. 7(b). This simple numerical experiment proves the working principle of the proposed device as an alternator and energy harvester.

The amplitude of the voltage can be linearly tuned by the skyrmion velocity [Fig. 7(c)], which is directly linked to the amplitude of the anisotropy and temperature gradients, and nonlinearly decreases with the height of the coil from the nanoring surface, as shown in Fig. 7(d).

To obtain a steady-state ac voltage signal, we can symmetrically deploy multiple skyrmions. Indeed, Fig. 7(e) depicts the output voltage due to the circulating motion of ten skyrmions.

In addition, a strategy to enhance the v_L amplitude is to use n(HM1/FM/HM2) ferromagnetic multilayers [8,9,24–29]. The asymmetric FM/HM1 and FM/HM2 interfaces enhance the IDMI leading to increased skyrmion stability. Hybrid (i.e., thickness-dependent) or homochiral (i.e., pure Néel) skyrmions extending through all FM layers can form in such a multilayer [92,93] as a trade-off among the anisotropy, magnetostatic, and IDMI energies. A skyrmion extending in all layers produces larger changes in the magnetic flux when it crosses the Faraday coil, leading to larger values of the voltage amplitude. Therefore, magnetic multilayers, instead of a single FM/HM bilayer, could be used to enhance the amplitude of the voltage pulse. In our study, we consider the physical parameters of Ref. [81] and the same geometrical parameters as in Fig. 1 for the FM layers. Successive FM layers are separated from each other by a 1-nm nonmagnetic layer. We relax a skyrmion as a function of the number of layers and we obtain a pure Néel skyrmion in all the cases. We compute the stray field and, from this, the v_L amplitude. Figure 7(f) shows that v_L linearly increases with the number of layers up to almost 0.5 μV.

Eventually, we wish to mention here that we are considering only one wrap in the Faraday coil, but the output voltage increases linearly with the number of wraps. For instance, with ten wraps, the voltage can be easily increased to more than 1 μV.

We also compare the simulation results of the skyrmion velocity in devices 2 and 3 with the developed Thiele formalism, given by Eq. (7) with $F(r) = F_K(r)$ for device 2 and with $F(r) = F_T(r)$ for device 3. For a skyrmion moving along the midcircle of the circular track, $r = R_0 + w/2$, the skyrmion velocity is calculated to be $v_{\mathrm{sk}} = 37$ m/s for device 2 and $v_{\mathrm{sk}} = 58$ m/s for device 3. These values are of the same order but higher than the simulation results ($v_{\mathrm{sk}} \approx 20$ m/s). We attribute the enhanced velocity in the analytical model to the absence of repulsive forces from the inner boundary of the nanoring when the skyrmion approaches. In particular, both gradient-induced forces $F_K(r)$ and $F_T(r)$ point in the inward radial direction, given the parameters used, and the edge force points in the outward radial direction. To account for this effect, we consider a fitting factor in the radial forces as $F(r) \rightarrow n_f F(r)$. The analytical calculations are in good agreement with the simulation results for $n_f \approx 0.5$ in device 2 and $n_f \approx 0.3$ in device 3, showing that the effect of the edge force has a key role in the skyrmion dynamics in those devices, as already shown for racetrack memories [39].

V. SUMMARY AND CONCLUSIONS

We demonstrate the versatile potential usages of skyrmions in nanorings by combining numerical micromagnetic simulations and analytical calculations based on the Thiele's equation. In particular, we propose and examine three applications that rely on the conversion of the skyrmion circulating motion into an electrical signal:

(1) A skyrmion clock, where the skyrmion motion driven by a radially flowing current generates periodic voltage pulses when the skyrmion pass below an MTJ. The frequency of the device can be tuned via current, material parameters, and number of skyrmions, reaching 200 MHz. This design allows for an intrinsic spatial synchronization of the clock frequency.

(2) A skyrmion alternator, where the skyrmion motion driven by an engineered anisotropy gradient (no electrical input) generates a voltage pulse close to the microvolt order due to the variation of the stray field through a Faraday coil. This idea is analogous to today's electrical generators, where the mechanical rotation of a rotor generates electrical voltage. We anticipate here that the gradient of other parameters can be used for the development of skyrmion alternators, such as magnetic field gradient and/or IDMI gradient.

(3) If the skyrmion motion is driven by thermal gradients, an energy harvester can be designed to partially recover the dissipated heat from a thermal source, such as a microprocessor.

Here, we summarize that experimental studies of those nanoring geometries can use low-damping FM materials, such as amorphous Co-Fe-B [60]. Stacks hosting hybrid skyrmions can be designed in such a way that the skyrmion Hall angle is reduced to optimize the performance of the nanoring-based devices in order to increase the skyrmion velocity. This can reflect not only in faster clocks, but also in an enhanced voltage generated by the skyrmion motion. In addition, we wish to stress that those skyrmion hosting materials can be integrated with MTJ stacks, as already demonstrated experimentally, making those device configurations more feasible [80].

At this stage of the research, it is not possible to perform a quantitative performance comparison between skyrmionic devices and existing clock solutions, since the development of skyrmionic devices is still at the level of critical function or proof-of-concept establishment (technological readiness level 3). From a qualitative point of view, the skyrmion-based clock implementation can be used to reduce the clock skew, enforcing the time synchronization between different parts of circuits. In other words, the skyrmion, being a soliton, can travel with a reduced distortion and can be used locally for the generation of the clock timing. Our vision for the skyrmion alternator is the possibility of creating a new generation of nano engines, hence the potential scalability at the nanoscale will be the advantage as compared with current technology.

The same idea of scalability at the nanoscale applies to the concept of energy harvesting. In this field, current technology is facing several challenges and skyrmion-based energy harvesting can give rise to an alternative direction in this research field [94].

ACKNOWLEDGMENTS

D.K. acknowledges financial support from the Special Account for Research of the School of Pedagogical and Technological Education through the program "Educational and Research Infrastructure Support" (Grant No. 52922) and hospitality by the Politecnico di Bari during the course of this work. The research has been supported by the project PRIN 2020LWPKH7 funded by the Italian Ministry of Research. R.T., V.P., M.C., and G.F. are with the PETASPIN team and thank the support of the PETASPIN association (www.petaspin.com). A.R. acknowledges the kind hospitality in the University of Messina, during the course of this work and financial support from CIP2022036. The work carried out at Tsinghua University was supported by the Basic Science Center Project of National Natural Science Foundation of China (NSFC Grant No. 52388201), National Key R&D Program of China (Grant No. 2022YFA1405100), the NSFC distinguished Young Scholar program (Grant No. 12225409), the Beijing Natural Science Foundation (Grant No. Z190009), the NSFC (Grants No. 52271181 and No. 51831005), the Tsinghua University Initiative Scientific Research Program and the Beijing Advanced Innovation Center for Future Chip (ICFC).

[1] G. Finocchio, F. Büttner, R. Tomasello, M. Carpentieri, and M. Kläui, Magnetic skyrmions: From fundamental to applications, J. Phys. D: Appl. Phys. **49**, 423001 (2016).

[2] G. Bonanno, *et al.*, in *Magnetic Skyrmions and Their Applications*, edited by G. Finocchio, C. Panagopoulos (Elsevier, Kidlington, Oxford, United Kingdom, 2021), pp. ix–xi.

[3] F. Büttner, I. Lemesh, and G. S. D. Beach, Theory of isolated magnetic skyrmions: From fundamentals to room temperature applications, Sci. Rep. **8**, 4464 (2018).

[4] A. Riveros, F. Tejo, J. Escrig, K. Y. Guslienko, and O. Chubykalo-Fesenko, Field-dependent energy barriers of magnetic Néel skyrmions in ultrathin circular nanodots, Phys. Rev. Appl. **16**, 014068 (2021).

[5] W. Legrand, D. Maccariello, N. Reyren, K. Garcia, C. Moutafis, C. Moreau-Luchaire, S. Collin, K. Bouzehouane,

V. Cros, and A. Fert, Room-temperature current-induced generation and motion of sub-100 nm skyrmions, Nano Lett. **17**, 2703 (2017).

[6] G. Yu, P. Upadhyaya, Q. Shao, H. Wu, G. Yin, X. Li, C. He, W. Jiang, X. Han, P. K. Amiri, and K. L. Wang, Room-temperature skyrmion shift device for memory application, Nano Lett. **17**, 261 (2017).

[7] K. Zeissler, S. Finizio, C. Barton, A. J. Huxtable, J. Massey, J. Raabe, A. V. Sadovnikov, S. A. Nikitov, R. Brearton, T. Hesjedal, G. van der Laan, M. C. Rosamond, E. H. Linfield, G. Burnell, and C. H. Marrows, Diameter-independent skyrmion Hall angle observed in chiral magnetic multilayers, Nat. Commun. **11**, 428 (2020).

[8] S. Woo, K. Litzius, B. Krüger, M. Y. Im, L. Caretta, K. Richter, M. Mann, A. Krone, R. M. Reeve, M. Weigand, P. Agrawal, I. Lemesh, M. A. Mawass, P. Fischer, M. Kläui, and G. S. D. Beach, Observation of room-temperature magnetic skyrmions and their current-driven dynamics in ultrathin metallic ferromagnets, Nat. Mater. **15**, 501 (2016).

[9] K. Litzius, I. Lemesh, B. Krüger, P. Bassirian, L. Caretta, K. Richter, F. Büttner, K. Sato, O. A. Tretiakov, J. Förster, R. M. Reeve, M. Weigand, I. Bykova, H. Stoll, G. Schütz, G. S. D. Beach, and M. Klaüi, Skyrmion Hall effect revealed by direct time-resolved x-ray microscopy, Nat. Phys. **13**, 170 (2017).

[10] W. Jiang, X. Zhang, G. Yu, W. Zhang, X. Wang, M. Benjamin Jungfleisch, J. E. Pearson, X. Cheng, O. Heinonen, K. L. Wang, Y. Zhou, A. Hoffmann, and S. G. E. Te Velthuis, Direct observation of the skyrmion Hall effect, Nat. Phys. **13**, 162 (2017).

[11] C. Wang, D. Xiao, X. Chen, Y. Zhou, and Y. Liu, Manipulating and trapping skyrmions by magnetic field gradients, New J. Phys. **19**, 083008 (2017).

[12] S. L. Zhang, W. W. Wang, D. M. Burn, H. Peng, H. Berger, A. Bauer, C. Pfleiderer, G. van der Laan, and T. Hesjedal, Manipulation of skyrmion motion by magnetic field gradients, Nat. Commun. **9**, 2115 (2018).

[13] A. Casiraghi, H. Corte-León, M. Vafaee, F. Garcia-Sanchez, G. Durin, M. Pasquale, G. Jakob, M. Kläui, and O. Kazakova, Individual skyrmion manipulation by local magnetic field gradients, Commun. Phys. **2**, 145 (2019).

[14] J. Liu, C. Song, L. Zhao, L. Cai, H. Feng, B. Zhao, M. Zhao, Y. Zhou, L. Fang, and W. Jiang, Manipulation of skyrmion by magnetic field gradients: A Stern–Gerlach-like experiment, Nano Lett. **23**, 4931 (2023).

[15] G. Yu, P. Upadhyaya, X. Li, W. Li, S. K. Kim, Y. Fan, K. L. Wong, Y. Tserkovnyak, P. K. Amiri, and K. L. Wang, Room-temperature creation and spin-orbit torque manipulation of skyrmions in thin films with engineered asymmetry, Nano Lett. **16**, 1981 (2016).

[16] R. Tomasello, S. Komineas, G. Siracusano, M. Carpentieri, and G. Finocchio, Chiral skyrmions in an anisotropy gradient, Phys. Rev. B **98**, 024421 (2018).

[17] Z. Wang, *et al.*, Thermal generation, manipulation and thermoelectric detection of skyrmions, Nat. Electron. **3**, 672 (2020).

[18] K. Litzius, J. Leliaert, P. Bassirian, D. Rodrigues, S. Kromin, I. Lemesh, J. Zazvorka, K. J. Lee, J. Mulkers, N. Kerber, D. Heinze, N. Keil, R. M. Reeve, M. Weigand, B. Van Waeyenberge, G. Schütz, K. Everschor-Sitte, G. S. D. Beach, and M. Kläui, The role of temperature and drive current in skyrmion dynamics, Nat. Electron. **3**, 30 (2020).

[19] E. Raimondo, E. Saugar, J. Barker, D. Rodrigues, A. Giordano, M. Carpentieri, W. Jiang, O. Chubykalo-Fesenko, R. Tomasello, and G. Finocchio, Temperature-gradient-driven magnetic skyrmion motion, Phys. Rev. Appl. **18**, 024062 (2022).

[20] X. Yu, D. Morikawa, Y. Tokunaga, M. Kubota, T. Kurumaji, H. Oike, M. Nakamura, F. Kagawa, Y. Taguchi, T. Arima, M. Kawasaki, and Y. Tokura, Current-induced nucleation and annihilation of magnetic skyrmions at room temperature in a chiral magnet, Adv. Mater. **29**, 1606178 (2017).

[21] W. Wang, D. Song, W. Wei, P. Nan, S. Zhang, B. Ge, M. Tian, J. Zang, and H. Du, Electrical manipulation of skyrmions in a chiral magnet, Nat. Commun. **13**, 1593 (2022).

[22] W. Jiang, P. Upadhyaya, W. Zhang, G. Yu, M. B. Jungfleisch, F. Y. Fradin, J. E. Pearson, Y. Tserkovnyak, K. L. Wang, O. Heinonen, S. G. E. Te Velthuis, and A. Hoffmann, Blowing magnetic skyrmion bubbles, Science **349**, 283 (2015).

[23] O. Boulle, J. Vogel, H. Yang, S. Pizzini, D. de S. Chaves, A. Locatelli, T. O. M. A. Sala, L. D. Buda-Prejbeanu, O. Klein, M. Belmeguenai, Y. Roussigné, A. Stashkevich, S. M. Chérif, L. Aballe, M. Foerster, M. Chshiev, S. Auffret, I. M. Miron, and G. Gaudin, Room temperature chiral magnetic skyrmion in ultrathin magnetic nanostructures, Nat. Nanotechnol. **11**, 449 (2016).

[24] C. Moreau-Luchaire, C. Moutafis, N. Reyren, J. Sampaio, C. A. F. Vaz, N. Van Horne, K. Bouzehouane, K. Garcia, C. Deranlot, P. Warnicke, P. Wohlhüter, J. M. George, M. Weigand, J. Raabe, V. Cros, and A. Fert, Additive interfacial chiral interaction in multilayers for stabilization of small individual skyrmions at room temperature, Nat. Nanotechnol. **11**, 444 (2016).

[25] A. Soumyanarayanan, M. Raju, A. L. G. Oyarce, A. K. C. Tan, M. Y. Im, A. P. Petrovic, P. Ho, K. H. Khoo, M. Tran, C. K. Gan, F. Ernult, and C. Panagopoulos, Tunable room-temperature magnetic skyrmions in Ir/Fe/Co/Pt multilayers, Nat. Mater. **16**, 898 (2017).

[26] F. Büttner, I. Lemesh, M. Schneider, B. Pfau, C. M. Günther, P. Hessing, J. Geilhufe, L. Caretta, D. Engel, B. Krüger, J. Viefhaus, S. Eisebitt, and G. S. D. Beach, Field-free deterministic ultrafast creation of magnetic skyrmions by spin–orbit torques, Nat. Nanotechnol. **12**, 1040 (2017).

[27] K. Zeissler, S. Finizio, K. Shahbazi, J. Massey, F. Al Ma'Mari, D. M. Bracher, A. Kleibert, M. C. Rosamond, E. H. Linfield, T. A. Moore, J. Raabe, G. Burnell, and C. H. Marrows, Discrete Hall resistivity contribution from Néel skyrmions in multilayer nanodiscs, Nat. Nanotechnol. **13**, 1161 (2018).

[28] D. Maccariello, W. Legrand, N. Reyren, K. Garcia, K. Bouzehouane, S. Collin, V. Cros, and A. Fert, Electrical detection of single magnetic skyrmions in metallic multilayers at room temperature, Nat. Nanotechnol. **13**, 233 (2018).

[29] W. Li, *et al.*, Anatomy of skyrmionic textures in magnetic multilayers, Adv. Mater. **31**, 1807683 (2019).

[30] S. Woo, K. M. Song, X. Zhang, Y. Zhou, M. Ezawa, X. Liu, S. Finizio, J. Raabe, N. J. Lee, S.-I. Kim, S.-Y. Park, Y. Kim, J.-Y. Kim, D. Lee, O. Lee, J. W. Choi, B.-C. Min, H. C. Koo, and J. Chang, Current-driven dynamics and inhibition of the skyrmion Hall effect of ferrimagnetic skyrmions in GdFeCo films, Nat. Commun. **9**, 959 (2018).

[31] L. Caretta, M. Mann, F. Büttner, K. Ueda, B. Pfau, C. M. Günther, P. Hessing, A. Churikova, C. Klose, M. Schneider, D. Engel, C. Marcus, D. Bono, K. Bagschik, S. Eisebitt, and G. S. D. Beach, Fast current-driven domain walls and small skyrmions in a compensated ferrimagnet, Nat. Nanotechnol. **13**, 1154 (2018).

[32] T. Dohi, S. DuttaGupta, S. Fukami, and H. Ohno, Formation and current-induced motion of synthetic antiferromagnetic skyrmion bubbles, Nat. Commun. **10**, 5153 (2019).

[33] W. Legrand, D. Maccariello, F. Ajejas, S. Collin, A. Vecchiola, K. Bouzehouane, N. Reyren, V. Cros, and A. Fert, Room-temperature stabilization of antiferromagnetic skyrmions in synthetic antiferromagnets, Nat. Mater. **19**, 34 (2020).

[34] R. Juge, *et al.*, Skyrmions in synthetic antiferromagnets and their nucleation via electrical current and ultra-fast laser illumination, Nat. Commun. **13**, 4807 (2022).

[35] A.-O. Mandru, O. Yıldırım, R. Tomasello, P. Heistracher, M. Penedo, A. Giordano, D. Suess, G. Finocchio, and H. J. Hug, Coexistence of distinct skyrmion phases observed in hybrid ferromagnetic/ferrimagnetic multilayers, Nat. Commun. **11**, 6365 (2020).

[36] T. Xu, Z. Chen, H.-A. Zhou, Z. Wang, Y. Dong, L. Aballe, M. Foerster, P. Gargiani, M. Valvidares, D. M. Bracher, T. Savchenko, A. Kleibert, R. Tomasello, G. Finocchio, S.-G. Je, M.-Y. Im, D. A. Muller, and W. Jiang, Imaging the spin chirality of ferrimagnetic Néel skyrmions stabilized on topological antiferromagnetic Mn_3Sn, Phys. Rev. Mater. **5**, 084406 (2021).

[37] O. Yıldırım, R. Tomasello, Y. Feng, G. Carlotti, S. Tacchi, P. M. Vaghefi, A. Giordano, T. Dutta, G. Finocchio, H. J. Hug, and A.-O. Mandru, Tuning the coexistence regime of incomplete and tubular skyrmions in ferromagnetic/ferrimagnetic/ferromagnetic trilayers, ACS Appl. Mater. Interfaces **14**, 34002 (2022).

[38] J. Sampaio, V. Cros, S. Rohart, A. Thiaville, and A. Fert, Nucleation, stability and current-induced motion of isolated magnetic skyrmions in nanostructures, Nat. Nanotechnol. **8**, 839 (2013).

[39] R. Tomasello, E. Martinez, R. Zivieri, L. Torres, M. Carpentieri, and G. Finocchio, A strategy for the design of skyrmion racetrack memories, Sci. Rep. **4**, 6784 (2014).

[40] X. Zhang, G. P. Zhao, H. Fangohr, J. P. Liu, W. X. Xia, J. Xia, and F. J. Morvan, Skyrmion-skyrmion and skyrmion-edge repulsions in skyrmion-based racetrack memory, Sci. Rep. **5**, 7643 (2015).

[41] F. Zheng, F. N. Rybakov, A. B. Borisov, D. Song, S. Wang, Z.-A. Li, H. Du, N. S. Kiselev, J. Caron, A. Kovács, M. Tian, Y. Zhang, S. Blügel, and R. E. Dunin-Borkowski, Experimental observation of chiral magnetic bobbers in B20-type FeGe, Nat. Nanotechnol. **13**, 451 (2018).

[42] R. Tomasello, A. Giordano, S. Chiappini, R. Zivieri, G. Siracusano, V. Puliafito, I. Medlej, A. La Corte, B. Azzerboni, M. Carpentieri, Z. Zeng, and G. Finocchio, Micromagnetic understanding of the skyrmion Hall angle current dependence in perpendicularly magnetized ferromagnets, Phys. Rev. B **98**, 224418 (2018).

[43] R. Juge, K. Bairagi, K. G. Rana, J. Vogel, M. Sall, D. Mailly, V. T. Pham, Q. Zhang, N. Sisodia, M. Foerster, L. Aballe, M. Belmeguenai, Y. Roussigné, S. Auffret, L. D. Buda-Prejbeanu, G. Gaudin, D. Ravelosona, and O. Boulle, Helium ions put magnetic skyrmions on the track, Nano Lett. **21**, 2989 (2021).

[44] P. Lai, G. P. Zhao, H. Tang, N. Ran, S. Q. Wu, J. Xia, X. Zhang, and Y. Zhou, An improved racetrack structure for transporting a skyrmion, Sci. Rep. **7**, 1 (2017).

[45] J. Barker and O. A. Tretiakov, Static and dynamical properties of antiferromagnetic skyrmions in the presence of applied current and temperature, Phys. Rev. Lett. **116**, 147203 (2016).

[46] H. Velkov, O. Gomonay, M. Beens, G. Schwiete, A. Brataas, J. Sinova, and R. A. Duine, Phenomenology of current-induced skyrmion motion in antiferromagnets, New J. Phys. **18**, 075016 (2016).

[47] X. Zhang, Y. Zhou, and M. Ezawa, Antiferromagnetic skyrmion: Stability, creation and manipulation, Sci. Rep. **6**, 24795 (2016).

[48] A. Salimath, F. Zhuo, R. Tomasello, G. Finocchio, and A. Manchon, Controlling the deformation of antiferromagnetic skyrmions in the high-velocity regime, Phys. Rev. B **101**, 24429 (2020).

[49] X. Zhang, Y. Zhou, and M. Ezawa, Magnetic bilayer-skyrmions without skyrmion Hall effect, Nat. Commun. **7**, 10293 (2016).

[50] R. Tomasello, V. Puliafito, E. Martinez, A. Manchon, M. Ricci, M. Carpentieri, and G. Finocchio, Performance of synthetic antiferromagnetic racetrack memory: Domain wall versus skyrmion, J. Phys. D: Appl. Phys. **50**, 325302 (2017).

[51] Y. Zhou, E. Iacocca, A. A. Awad, R. K. Dumas, F. C. Zhang, H. B. Braun, and J. Åkerman, Dynamically stabilized magnetic skyrmions, Nat. Commun. **6**, 8193 (2015).

[52] M. Carpentieri, R. Tomasello, R. Zivieri, and G. Finocchio, Topological, non-topological and instanton droplets driven by spin-transfer torque in materials with perpendicular magnetic anisotropy and Dzyaloshinskii-Moriya interaction, Sci. Rep. **5**, 16184 (2015).

[53] S. Zhang, J. Wang, Q. Zheng, Q. Zhu, X. Liu, S. Chen, C. Jin, Q. Liu, C. Jia, and D. Xue, Current-induced magnetic skyrmions oscillator, New J. Phys. **17**, 023061 (2015).

[54] F. Garcia-Sanchez, J. Sampaio, N. Reyren, V. Cros, and J.-V. Kim, A skyrmion-based spin-torque nano-oscillator, New J. Phys. **18**, 075011 (2016).

[55] G. Finocchio, M. Ricci, R. Tomasello, A. Giordano, M. Lanuzza, V. Puliafito, P. Burrascano, B. Azzerboni, and M. Carpentieri, Skyrmion based microwave detectors and harvesting, Appl. Phys. Lett. **107**, 262401 (2015).

[56] X. Zhang, M. Ezawa, and Y. Zhou, Magnetic skyrmion logic gates: Conversion, duplication and merging of skyrmions, Sci. Rep. **5**, 9400 (2015).

[57] B. W. Walker, C. Cui, F. Garcia-Sanchez, J. A. C. Incorvia, X. Hu, and J. S. Friedman, Skyrmion logic clocked via

voltage-controlled magnetic anisotropy, Appl. Phys. Lett. **118**, 192404 (2021).

[58] N. Sisodia, J. Pelloux-Prayer, L. D. Buda-Prejbeanu, L. Anghel, G. Gaudin, and O. Boulle, Programmable skyrmion logic gates based on skyrmion tunneling, Phys. Rev. Appl. **17**, 064035 (2022).

[59] D. Pinna, F. Abreu Araujo, J. V. Kim, V. Cros, D. Querlioz, P. Bessiere, J. Droulez, and J. Grollier, Skyrmion gas manipulation for probabilistic computing, Phys. Rev. Appl. **9**, 64018 (2018).

[60] J. Zázvorka, F. Jakobs, D. Heinze, N. Keil, S. Kromin, S. Jaiswal, K. Litzius, G. Jakob, P. Virnau, D. Pinna, K. Everschor-Sitte, L. Rózsa, A. Donges, U. Nowak, and M. Kläui, Thermal skyrmion diffusion used in a reshuffler device, Nat. Nanotechnol. **14**, 658 (2019).

[61] D. Prychynenko, M. Sitte, K. Litzius, B. Krüger, G. Bourianoff, M. Kläui, J. Sinova, and K. Everschor-Sitte, Magnetic skyrmion as a nonlinear resistive element: A potential building block for reservoir computing, Phys. Rev. Appl. **9**, 14034 (2018).

[62] G. Bourianoff, D. Pinna, M. Sitte, and K. Everschor-Sitte, Potential implementation of reservoir computing models based on magnetic skyrmions, AIP Adv. **8**, 055602 (2018).

[63] D. Pinna, G. Bourianoff, and K. Everschor-Sitte, Reservoir computing with random skyrmion textures, Phys. Rev. Appl. **14**, 054020 (2020).

[64] Y. Yao, X. Chen, W. Kang, Y. Zhang, and W. Zhao, Thermal Brownian motion of skyrmion for true random number generation, IEEE Trans. Electron Devices **67**, 2553 (2020).

[65] S. Luo, M. Song, X. Li, Y. Zhang, J. Hong, X. Yang, X. Zou, N. Xu, and L. You, Reconfigurable skyrmion logic gates, Nano Lett. **18**, 1180 (2018).

[66] M. Chauwin, X. Hu, F. Garcia-Sanchez, N. Betrabet, A. Paler, C. Moutafis, and J. S. Friedman, Skyrmion logic system for large-scale reversible computation, Phys. Rev. Appl. **12**, 064053 (2019).

[67] H. Zhang, D. Zhu, W. Kang, Y. Zhang, and W. Zhao, Stochastic computing implemented by skyrmionic logic devices, Phys. Rev. Appl. **13**, 054049 (2020).

[68] Y. Huang, W. Kang, X. Zhang, Y. Zhou, and W. Zhao, Magnetic skyrmion-based synaptic devices, Nanotechnology **28**, 08LT02 (2017).

[69] K. M. Song, J.-S. Jeong, B. Pan, X. Zhang, J. Xia, S. Cha, T.-E. Park, K. Kim, S. Finizio, J. Raabe, J. Chang, Y. Zhou, W. Zhao, W. Kang, H. Ju, and S. Woo, Skyrmion-based artificial synapses for neuromorphic computing, Nat. Electron. **3**, 148 (2020).

[70] S. Li, W. Kang, Y. Huang, X. Zhang, Y. Zhou, and W. Zhao, Magnetic skyrmion-based artificial neuron device, Nanotechnology **28**, 31LT01 (2017).

[71] X. Chen, W. Kang, D. Zhu, X. Zhang, N. Lei, Y. Zhang, Y. Zhou, and W. Zhao, A compact skyrmionic leaky–integrate–fire spiking neuron device, Nanoscale **10**, 6139 (2018).

[72] B. Pan, D. Zhang, X. Zhang, H. Wang, J. Bai, J. Yang, Y. Zhang, W. Kang, and W. Zhao, Skyrmion-induced memristive magnetic tunnel junction for ternary neural network, IEEE J. Electron Devices Soc. **7**, 529 (2019).

[73] S. Luo, N. Xu, Z. Guo, Y. Zhang, J. Hong, and L. You, Voltage-controlled skyrmion memristor for energy-efficient synapse applications, IEEE Electron Device Lett. **40**, 635 (2019).

[74] Z. Yu, M. Shen, Z. Zeng, S. Liang, Y. Liu, M. Chen, Z. Zhang, Z. Lu, L. You, X. Yang, Y. Zhang, and R. Xiong, Voltage-controlled skyrmion-based nanodevices for neuromorphic computing using a synthetic antiferromagnet, Nanoscale Adv. **2**, 1309 (2020).

[75] R. Tomasello, A. Giordano, F. Garescì, G. Siracusano, S. De Caro, C. Ciminelli, M. Carpentieri, and G. Finocchio, Role of magnetic skyrmions for the solution of the shortest path problem, J. Magn. Magn. Mater. **532**, 167977 (2021).

[76] B. Paikaray, M. Kuchibhotla, C. Murapaka, and A. Haldar, Skyrmion dynamics in concentric and eccentric nano-ring structures, IEEE Trans. Magn. **58**, 4300406 (2022).

[77] M. Ponsudana, R. Amuda, R. Madhumathi, A. Brinda, and N. Kanimozhi, Confinement of stable skyrmionium and skyrmion state in ultrathin nanoring, Phys. B: Condens. Matter **618**, 413144 (2021).

[78] M. Raju, A. Yagil, A. Soumyanarayanan, A. K. C. Tan, A. Almoalem, F. Ma, O. M. Auslaender, and C. Panagopoulos, The evolution of skyrmions in Ir/Fe/Co/Pt multilayers and their topological Hall signature, Nat. Commun. **10**, 696 (2019).

[79] S. Li, A. Du, Y. Wang, X. Wang, X. Zhang, H. Cheng, W. Cai, S. Lu, K. Cao, B. Pan, N. Lei, W. Kang, J. Liu, A. Fert, Z. Hou, and W. Zhao, Experimental demonstration of skyrmionic magnetic tunnel junction at room temperature, Sci. Bull. **67**, 691 (2022).

[80] Y. Guang, *et al.*, Electrical detection of magnetic skyrmions in a magnetic tunnel junction, Adv. Electron. Mater. **9**, 2200570 (2023).

[81] R. Tomasello, K. Y. Guslienko, M. Ricci, A. Giordano, J. Barker, M. Carpentieri, O. Chubykalo-Fesenko, and G. Finocchio, Origin of temperature and field dependence of magnetic skyrmion size in ultrathin nanodots, Phys. Rev. B **97**, 060402 (2018).

[82] R. Tomasello, M. Ricci, P. Burrascano, V. Puliafito, M. Carpentieri, and G. Finocchio, Electrical detection of single magnetic skyrmion at room temperature, AIP Adv. **7**, 056022 (2017).

[83] A. Giordano, G. Finocchio, L. Torres, M. Carpentieri, and B. Azzerboni, Semi-implicit integration scheme for Landau-Lifshitz-Gilbert-Slonczewski equation, J. Appl. Phys. **111**, 2010 (2012).

[84] R. Tomasello, M. Carpentieri, and G. Finocchio, Influence of the Dzyaloshinskii-Moriya interaction on the spin-torque diode effect, J. Appl. Phys. **115**, 17C730 (2014).

[85] A. A. Thiele, Steady-state motion of magnetic domains, Phys. Rev. Lett. **30**, 230 (1973).

[86] S. Ikeda, K. Miura, H. Yamamoto, K. Mizunuma, H. D. Gan, M. Endo, S. Kanai, J. Hayakawa, F. Matsukura, and H. Ohno, A perpendicular-anisotropy CoFeB–MgO magnetic tunnel junction, Nat. Mater. **9**, 721 (2010).

[87] M. Belmeguenai, J.-P. Adam, Y. Roussigné, S. Eimer, T. Devolder, J.-V. Kim, S. Mourad Cherif, A. Stashkevich, and A. Thiaville, Interfacial Dzyaloshinskii-Moriya interaction in perpendicularly magnetized Pt/Co/AlOx ultrathin films measured by Brillouin light spectroscopy, Phys. Rev. B **91**, 180405(R) (2015).

[88] J. Von Kim and M. W. Yoo, Current-driven skyrmion dynamics in disordered films, Appl. Phys. Lett. **110**, 132404 (2017).
[89] C. Schütte, J. Iwasaki, A. Rosch, and N. Nagaosa, Inertia, diffusion, and dynamics of a driven skyrmion, Phys. Rev. B **90**, 174434 (2014).
[90] W. F. Brown, Thermal fluctuations of a single-domain particle, Phys. Rev. **130**, 1677 (1963).
[91] G. Finocchio, I. N. Krivorotov, X. Cheng, L. Torres, and B. Azzerboni, Micromagnetic understanding of stochastic resonance driven by spin-transfer-torque, Phys. Rev. B **83**, 134402 (2011).
[92] W. Legrand, J.-Y. Chauleau, D. Maccariello, N. Reyren, S. Collin, K. Bouzehouane, N. Jaouen, V. Cros, and A. Fert, Hybrid chiral domain walls and skyrmions in magnetic multilayers, Sci. Adv. **4**, eaat0415 (2018).
[93] N. K. Duong, R. Tomasello, M. Raju, A. P. Petrovíc, S. Chiappini, G. Finocchio, and C. Panagopoulos, Magnetization reversal signatures of hybrid and pure Néel skyrmions in thin film multilayers, APL Mater. **8**, 111112 (2020).
[94] J. D. Phillips, Energy harvesting in nanosystems: Powering the next generation of Internet-of-things, Front. Nanotechnol. **3**, 633931 (2021).